Kinetic electron closures for electromagnetic simulation of drift and shear-Alfvén waves (II)

Bruce I. Cohen, Andris M. Dimits, and William M. Nevins

University of California Lawrence Livermore National Laboratory

Livermore, California 94550

Yang Chen and Scott Parker

Department of Physics, University of Colorado at Boulder

Boulder, CO 80309

Abstract

An electromagnetic hybrid scheme (fluid electrons and gyrokinetic ions) is elaborated in example calculations and extended to toroidal geometry. The scheme includes a kinetic electron closure valid for $\beta_e > m_e/m_i$ (β_e is the ratio of the plasma electron pressure to the magnetic field energy density). The new scheme incorporates partially linearized (δf) drift-kinetic electrons whose pressure and number density moments are used to close the fluid momentum equation for the electron fluid (Ohm's law). The test cases used are small-amplitude kinetic shear-Alfvén waves with electron Landau damping, the ion-temperature-gradient instability, and the collisionless drift instability (universal mode) in an unsheared slab as a function of the plasma β_e. Attention is given to resolution and convergence issues in simulations of turbulent steady states.

PACS numbers: 52.65.-y, 52.65.Tt, 52.35.Qz

I. INTRODUCTION

Nonadiabatic electron effects significantly modify the stability and concomitant turbulent transport of drift-waves in tokamaks. Incorporating electron kinetic and electromagnetic effects into gyrokinetic particle-in-cell drift-wave turbulence simulations is computationally challenging: electrons and electromagnetics introduce additional time and space scales that alter numerical stability, increase temporal and spatial resolution requirements and, hence, increase the computational burden. In previous work[1] we extended the electromagnetic hybrid scheme of Chen and Parker[2] (fluid electrons and gyrokinetic ions) to include a kinetic electron closure valid for $\beta_e m_i / m_e \geq 1$ where $\beta_e = 4\pi n_e T_e / B^2$, T_e is the electron temperature, and B is the magnetic field strength. We introduced a new closure scheme that makes particle simulation of electromagnetic drift-wave turbulence with drift-kinetic electrons and gyrokinetic ions tractable with realistic mass ratios and realistic β_e.

The new algorithm incorporates partially linearized[3,4] δf drift-kinetic electrons whose pressure and number density moments are used to close the fluid momentum equation for the electron fluid (Ohm's law). Comparisons were made in Ref. 1 between the results of three hybrid schemes with kinetic electron closures and a conventional δf algorithm for drift-kinetic electrons and gyrokinetic ions in a two-dimensional slab model. The test cases used were small-amplitude kinetic shear-Alfvén waves with electron Landau damping, the ion-temperature-gradient instability, and the collisionless drift instability (universal mode) in an unsheared slab as a function of β_e. The hybrid schemes have the desirable properties that they do *not* require that the mesh size perpendicular to the applied magnetic field be smaller than the collisionless skin depth c/ω_{pe} and naturally accommodate zonal flow physics (radial modes[5]) with non-adiabatic

electron effects. The best of the new hybrid schemes uses a variation of the split-weight scheme introduced by Manuilsky and Lee.[6] In this case the electron distribution function f_e is given by

$$f_e = f_M(\vec{\mathbf{x}}, \vec{\mathbf{v}}) + (\delta n_e^{(0)} / n_0) f_M(\vec{\mathbf{x}}, \vec{\mathbf{v}}) + h_e(\vec{\mathbf{x}}, \vec{\mathbf{v}}), \quad (1)$$

where f_M is a Maxwellian velocity distribution function including possible equilibrium temperature and density gradients, n_0 is the equilibrium electron density, $\delta n_e^{(0)}$ is the lowest-order fluid approximation to the total electron density perturbation (more explicitly defined in Sec. II), and h_e is the non-adiabatic part of the electron density perturbation determined using a variant of the δf method. The split-weight algorithm is found to be efficacious in that statistical noise arising from the particle representation is relegated to the relatively small h_e term in Eq.(1). The Hybrid II algorithm introduced in Ref. 1 gives very good results for $\beta_e m_i / m_e \geq 1$ and poor results in the opposite limit.

The new hybrid scheme departs from earlier work[7,8,9,10] in several respects. The research of Reynders[7] and Cummings[8] did not use split-weight methods nor hybrid techniques, and their algorithms could not efficiently address plasma conditions for which $\beta_e m_i / m_e >> 1$. The research of Cohen and Dimits[9] used implicit δf methods, did not use split-weight methods, and did not address $\beta_e m_i / m_e >> 1$ plasma conditions. Chen and Parker have modeled kinetic electrons in three-dimensional toroidal simulations using parallel canonical momentum and a variant of the split-weight scheme; however, their simulations were still limited to $\beta_e m_i / m_e \leq 1$. The approach taken in our extended hybrid algorithm resembles in some respects the work of Lin and Chen[11] who introduced a new split-weight algorithm and applied it to the propagation of small-amplitude shear-Alfvén waves in a uniform plasma. Our extended hybrid algorithm accommodates the nonlinear generation of zonal flows (radial modes[5]) not addressed in the work of Lin and Chen.[11] The work presented here illustrates the Hybrid II algorithm in additional test

cases addressing accuracy and convergence in nonlinear simulations of drift-type turbulence and extends the formulation of the algorithm to a toroidal flux-tube geometry.

The remainder of the paper is organized as follows. In Section II we review the Hybrid II kinetic extension of the Chen and Parker hybrid model.[1,2] Section III reviews the results of the Hybrid II algorithm in simulating the propagation and damping of small-amplitude shear-Alfvén waves, small-amplitude collisionless drift and ion-temperature gradient (ITG) instabilities, and simulation results for many-mode simulation of the linear growth and nonlinear saturation in two spatial dimensions of an ITG instability. The toroidal flux-tube extension of the Hybrid II algorithm is given in Sec. IV. In Section V we present simulation results that examine the accuracy and convergence of the simulation results with respect to time step, size of the simulation box, and particle statistics, and discuss the general accuracy and stability characteristics of the Hybrid II algorithm. In Section VI we conclude.

II. ELECTROMAGNETIC ALGORITHM FOR KINETIC SIMULATION OF DRIFT AND SHEAR-ALFVÉN WAVES

In this section we describe the basic ingredients of the Hybrid II algorithm in a slab configuration. Ions are described as δf gyrokinetic particles, and their trajectories are advanced with a predictor-corrector scheme using a time step Δt that is the same as that used in the solution of the field equations. Electrons are described jointly by fluid equations generated by taking moments of the drift-kinetic equations and as δf drift-kinetic particles, whose trajectories are also advanced with a predictor-corrector scheme using the same time step as that for the ions. Ion currents and charge densities, and electron parallel and perpendicular pressure moments and the electron charge density are accumulated from the particles at each Δt and used in the fluid

equations, Ampere's law, and the quasi-neutrality equation to determine the electrostatic potential and the parallel vector potential.

The ions and electrons satisfy the gyrokinetic reduced Vlasov-Maxwell equations[8,10,12] with the following orderings:

$$\frac{\delta f_{e,i}}{F_M^{e,i}} \sim \frac{e\phi}{T} \sim \frac{|\delta\vec{\mathbf{B}}|}{B} \sim \frac{\omega}{\Omega_i} \sim \frac{\rho_i}{L} \sim \varepsilon << 1 \quad \text{and} \quad L \sim L_{\|}, \tag{2}$$

where $\rho_i \equiv v_i / \Omega_i$ is the ion Larmor radius defined as the ratio of the ion thermal velocity to the ion cyclotron frequency, $\Omega_i = qB/m_i c$, $v_i = (T_i/m_i)^{1/2}$, q, m_i, and T_i, respectively, are the ion charge, mass, and temperature; c is the speed of light, B is the equilibrium magnetic-field strength, $\delta\vec{\mathbf{B}}$ is the perturbed magnetic field, ϕ is the electrostatic potential, ω is the frequency of the field perturbation, L is a characteristic perpendicular equilibrium scale length of the system, and $L_{\|}$ is the characteristic parallel wavelength of the perturbation. We use a multi-scale treatment throughout.[1,4,5] The electric and magnetic fields are given by

$$\vec{\mathbf{E}} = -\vec{\nabla}\phi - c^{-1}\partial\vec{\mathbf{A}}_{\|}/\partial t, \vec{\mathbf{B}} = \vec{\mathbf{B}}_0 + \nabla \times A_z\hat{\mathbf{z}} = B_0\hat{\mathbf{z}} + B_y^{(0)}\hat{\mathbf{y}} + \nabla \times A_z\hat{\mathbf{z}}\,. \tag{3}$$

The ion and electron kinetic distribution functions are represented by

$$f_{e,i} = F_M^{e,i} + \delta f_{e,i}(\vec{\mathbf{x}},\vec{\mathbf{v}},t), \quad \delta h_e, \delta f_i = \sum_i w_i^{e,i}\delta(\vec{\mathbf{x}} - \vec{\mathbf{x}}_i)\delta(\vec{\mathbf{v}} - \vec{\mathbf{v}}_i), \tag{4}$$

where $\delta f_e = (\delta n_e^{(0)}/n_{0e}) f_M(\vec{\mathbf{x}},\vec{\mathbf{v}}) + h_e(\vec{\mathbf{x}},\vec{\mathbf{v}})$ using Eq.(1). The equilibrium distribution functions $F_M^{e,i}$ are Maxwellians in the parallel velocity and the magnetic moment. The marker particles in our simulations are initialized in velocity space using a Maxwellian distribution. The partially linearized gyrokinetic ion and drift-kinetic electron Vlasov equations for a plasma with weak magnetic shear in slab geometry are[4,13,14]

$$\frac{\partial \delta f_i}{\partial t} + v_{\|}\hat{\mathbf{b}}\cdot\frac{\partial \delta f_i}{\partial \vec{\mathbf{R}}} - \frac{c}{B}\frac{\partial}{\partial \vec{\mathbf{R}}}\left(\frac{\partial \bar{\phi}}{\partial \vec{\mathbf{R}}}\times\hat{\mathbf{b}}\right)\cdot\nabla\delta f_i = -\frac{v_{\|}}{T_i}\left(\frac{\partial \bar{\phi}}{\partial \vec{\mathbf{R}}}\cdot\hat{\mathbf{b}}\right)F_M^i - \kappa_i\left(\frac{c}{B}\frac{\partial \bar{\phi}}{\partial y} - \frac{v_{\|}}{B}\frac{\partial \bar{A}_z}{\partial y}\right)F_M^i \qquad (5)$$

$$\frac{\partial \delta f_e}{\partial t} + v_{\|}\hat{\mathbf{b}}\cdot\frac{\partial \delta f_e}{\partial \vec{\mathbf{R}}} - \frac{c}{B}\frac{\partial}{\partial \vec{\mathbf{R}}}\left(\frac{\partial \phi}{\partial \vec{\mathbf{R}}}\times\hat{\mathbf{b}}\right)\cdot\nabla\delta f_e = \frac{v_{\|}}{T_e}\left(\frac{\partial \phi}{\partial \vec{\mathbf{R}}}\cdot\hat{\mathbf{b}}\right)F_M^e - \kappa_e\left(\frac{c}{B}\frac{\partial \phi}{\partial y} - \frac{v_{\|}}{B}\frac{\partial A_z}{\partial y}\right)F_M^e \qquad (6)$$

where $\hat{\mathbf{b}} = \hat{\mathbf{z}} + \hat{\mathbf{y}}B_y^{(0)}/B_0 + \quad \times A_z\hat{\mathbf{z}}/B_0$, $\hat{\mathbf{b}}^{(0)} = \hat{\mathbf{z}} + \hat{\mathbf{y}}B_y^{(0)}/B_0$,

$\kappa_s \equiv -\ \ln F_M^s = \kappa_{ns}\left[1 + \eta_s\left(v^2/2v_s^2 - 3/2\right)\right]$, κ_{ns} is the magnitude of the density gradient for species s, $\eta_s \equiv d\ln T_s / d\ln n_s$,

$$\bar{\phi} \equiv \frac{1}{2\pi}\oint d\hat{\rho}\,\phi(\vec{\mathbf{R}} + \vec{\rho}) \qquad (7)$$

and analogously for $\bar{E}$, etc., $\vec{\mathbf{R}} \equiv \vec{\mathbf{x}} - \vec{\rho}$, $\vec{\rho} \equiv \vec{\mathbf{v}} \quad \times \hat{\mathbf{b}}/\Omega_i$, $\hat{\rho}$ is a unit vector in the direction of $\vec{\rho}$ (the integral in Eq.(7) is an integral around the Larmor orbit with respect to the gyrophase angle), $\vec{\mathbf{x}}$ is the particle positon vector, $\vec{\mathbf{v}}$ is the perpendicular velocity, $\delta f_{e,i}(\vec{\mathbf{R}}, \mu, v_{\|}, t)$ is the gyroaveraged perturbed distribution function, and $\mu \equiv v^2/2$. The electrons have small Larmor radius.

Partial linearization is a simplifying ansatz. The justification for the partial linearization for the ions has been addressed in the literature for low-frequency drift-type instabilities satisfying the orderings laid out in Eq.(2) (for example, see Refs. 4, 8, 13 and 14). Linear wave-particle resonances for both electrons and ions are retained in the partially linearized equation set. Moreover, the important **E×B** kinetic trapping nonlinearity and the associated nonlinear wave-particle interaction are retained for both species. Because the orderings in Eq.(2) imply, among other things, that $k_{\|} << k$ and $k\ \rho_i \approx O(1)$, for the low-frequency drift-type instabilities of interest here the E×B velocity nonlinearity in kinetic equation dominates the nonlinearity

associated with the parallel electric field and the velocity derivative of the perturbed distribution function for the ions. However, the validity of partial linearization for the electrons is not so clear. An algorithm including the parallel nonlinearity for the electrons will have more general validity. The inclusion of the parallel nonlinearity does *not* profoundly alter the gyrokinetic/drift-kinetic particle algorithms as demonstrated by Parker, Lee, and others (see Refs. 8 and 10 for examples). One consequence of including the parallel nonlinearity is that $v_{\|}$ is no longer a constant of the motion. For simplicity in this paper exploring a new algorithm, we have suppressed the parallel electric-field nonlinearity in both the ions and electrons. The relative importance of the electron parallel electric-field nonlinearity needs investigation, and we will include the electron parallel electric-field nonlinearity in future simulation work.

The electrostatic potential ϕ is given by the gyrokinetic Poisson equation, which for a single-ion species (species subscript *i* and singly charged), is given by

$$\nabla^2\phi - \frac{\tau(\phi - \tilde{\bar{\phi}})}{\lambda_D^2} = 4\pi e\left(\delta\bar{n}_i - \delta n_e\right), \tag{8}$$

where $\tilde{\bar{\phi}}(\vec{\mathbf{x}}) \equiv \frac{1}{2\pi}\int d\mu d\hat{\rho}\,\bar{\phi}(\vec{\mathbf{x}} - \vec{\rho}), \tau \equiv T_e / T_i$, $\lambda_D^2 \equiv T_e / 4\pi n_{0e} e^2$ is the square of the electron Debye length, n_{0e} is the unperturbed electron on density, $\delta\bar{n}_i$ is the gyroaveraged perturbed ion density, δn_e is the perturbed electron density, and for simplicity we have assumed that the ions are singly charged. The angle averages indicated in $\delta\bar{n}_i$ and $\bar{\phi}$ are replaced by averages over four points on the ion Larmor orbit. The field interpolations from the grid to the particles and the deposition of distribution function moments from the particles onto the grid involve spatial weighting functions. Ampere's law relates the parallel component of the vector potential and the parallel currents:

$$-\nabla_\perp^2 A_z = \frac{4\pi}{c}\left(j_{e\|} + j_{i\|}\right), \tag{9}$$

and the ion current is computed to lowest significant order from the ion distribution function, $j_{i\|} = \int d\mu dv_\| v_\| \delta f_i$. We postpone discussion of the electron parallel current. The equilibrium density gradients are in the *x* direction, and the unperturbed magnetic field has its principal component in the *z* direction with a small component in the *y* direction. With no magnetic shear $B_y^{(0)}$ is a constant, and with shear $B_y^{(0)} = B_0(x - x_0)/L_s$, where L_s is the magnetic shear length. In the unsheared slab, all quantities are subject to periodic boundary conditions. With magnetic shear, the electric and vector potentials satisfy Dirichlet boundary conditions in *x* and are periodic in *y*.[7-9]

The gyrokinetic ion particle equations of motion are given by

$$d\vec{\mathbf{x}}/dt = \vec{\mathbf{v}} \qquad \vec{\mathbf{v}} = \vec{\mathbf{v}}_\| + \left\langle \vec{\mathbf{v}}_{\mathbf{E}\times\mathbf{B}} \right\rangle \tag{10}$$

$$\frac{dw_j^i}{dt} = \left\langle \frac{ev_\|}{T_e}\vec{\mathbf{E}}\cdot\hat{\mathbf{b}} \right\rangle - \kappa_i \left\langle \frac{c}{B}\frac{\partial\phi}{\partial y} \right\rangle - \left\langle \frac{v_\|\tilde{B}_x}{B} \right\rangle, \tag{11}$$

where the angle brackets in the right sides of Eq.(10) and (11) indicate a four-point average around the ion Larmor orbit, $\nabla_\|^{(0)} \equiv \hat{\mathbf{b}}^{(0)}\cdot\nabla$, and w_j^i are the ion particle weights.

For the electrons we compute the parallel velocity moment of the drift-kinetic equation and obtain the modified electron momentum equation (Ohm's law) following the approach introduced in Ref. 2 and rigorously justified in Ref. 16 for the orderings in Eq.(2):

$$en_{0e}\vec{E}\cdot\hat{b} = -\nabla_\| P_{\|e} - n_{0e}m_e(\partial/\partial t + \vec{v}_{E\times B}\cdot\nabla)u_{\|e}, \tag{12}$$

where $\nabla_{\|} \equiv \hat{\mathbf{b}} \cdot \nabla$, with

$$\nabla_{\|} P_{\|e} = \nabla_{\|} P_{\|e}^{(0)} + T_{\|e}^{(0)} \nabla_{\|} \delta n_e^{(0)} + n_{0e} \nabla_{\|} \delta T_{\|e} = \nabla_{\|} P_{\|e}^{(0)} + T_{\|e}^{(0)} \nabla_{\|} (\delta n_e - \Delta n_e^K) + n_{0e} \nabla_{\|} \delta T_{\|e}, \quad (13)$$

using Eq.(1) to make the substitution $\delta n_e^{(0)} = \delta n_e - \Delta n_e^K$, where $\delta n_e^{(0)}$ is the lowest-order fluid component of the perturbed electron density, $\delta n_e = \delta n_e^{(0)} + \Delta n_e^K$ is the total perturbed electron density including kinetic corrections consistent with the density moment of Eq.(1), and $\Delta n_e^K = \int d^3\mathbf{v} h_e$ is the split-weight kinetic electron *increment* to the charge density, $\nabla_{\|}(T_{\|e}^{(eq)} + \delta T_{\|e}) = 0$ is imposed as a constraint on the fluid electron temperature representation,[16] $T_{\|e}^{(eq)}$ is the equilibrium temperature (including gradients), $P_{\|e}^{(0)} = n_e^{(0)} T_{\|e}^{(eq)}$, $n_e^{(0)}$ is the equilibrium density (including gradients), $T_{\|e}^{(0)}$ is a constant. Non-adiabatic kinetic corrections to Eqs.(12) and (13) derived from the second parallel velocity moment of Eq.(1) are higher order in $(\omega / k_{\|} v_e)^2$ than are the terms coming from the adiabatic response. The representation of the perturbed electron density as an expansion around the fluid density is completely analogous to Ref. 11. In our formulation the expansion parameter is $\left| \Delta n_e^K / \delta n_e^{(0)} \right| << 1$.

Ohm's law, Eq.(12) using (13) for the pressure gradient, is used to obtain $E_{\|}$. This electric field together with $\partial A_z / \partial t = c(\vec{\mathbf{E}} + \nabla\phi) \cdot \hat{\mathbf{b}}^{(0)}$ is used to advance A_z in time. With the updated A_z, Ampere's law determines the parallel electron current:

$$n_{0e} u_{\|e} = \frac{c}{4\pi e} \nabla^2 A_z + \bar{\Gamma}_{\|i}, \quad (14)$$

where $\bar{\Gamma}_{||i}$ is the gyrokinetic parallel ion current per unit charge. The velocity integral of the electron drift-kinetic equation yields the electron continuity equation which provides the prescription for advancing the total electron density ahead in time:

$$\frac{\partial \delta n_e}{\partial t} + n_{0e}(\vec{\mathbf{B}}^{(0)} + \delta\vec{\mathbf{B}}\ ) \quad \frac{u_{||e}}{B} + \vec{\mathbf{v}}_{\mathbf{E}\times\mathbf{B}} \quad n_e = 0 \tag{15}$$

where $n_e = n_e^{(0)} + \delta n_e$. Curvature and gradient-B drifts and toroidal effects are added in Sec. IV.[2,16] The electrostatic potential is obtained from the quasi-neutral form of Eq.(8) suppressing the first term on the left side of Eq.(8) and using the updated total electron and ion charge densities. The evolution of the drift-kinetic electron positions, velocities, and weights deduced from Eq.(6) is computed with a predictor-corrector time integration (after using Eqs.(12), (13), and (15)),

$$d\vec{\mathbf{x}} / dt = \vec{\mathbf{v}} \quad \vec{\mathbf{v}} = \vec{\mathbf{v}}_{||} + \vec{\mathbf{v}}_{\mathbf{E}\times\mathbf{B}} \tag{16}$$

$$\frac{dw_j^e}{dt} = \vec{\kappa}_e \ \ \vec{\mathbf{v}}_{\mathbf{E}\times\mathbf{B}} + (\kappa_e - \kappa_{ne})v_{||}\frac{\delta B_x}{B_0} - \frac{\partial \delta n_e^{(0)} / n_{0e}}{\partial t} - \vec{\mathbf{v}}_{\mathbf{E}\times\mathbf{B}} \quad \delta n_e^{(0)} / n_{0e} + (v_{||}/v_e^2)(\frac{\partial}{\partial t} + \vec{\mathbf{v}}_{\mathbf{E}\times\mathbf{B}} \quad)u_{||e}$$

$$\approx (\vec{\mathbf{v}}_{\mathbf{E}\times\mathbf{B}} \ \ \hat{\mathbf{x}} + v_{||}\frac{\delta B_x}{B_0})\kappa_{Te}(\frac{v^2}{v_e^2} - \frac{3}{2}) + \ \ _{||}u_{||e} + (v_{||}/v_e^2)(\frac{\partial}{\partial t} + \vec{\mathbf{v}}_{\mathbf{E}\times\mathbf{B}} \quad)u_{||e}, \tag{17}$$

where we have used the lowest-order approximation $\delta n_e \approx \delta n_e^{(0)}$ in the continuity equation employed in obtaining the final expression on the right side of (17), which makes explicit use of the small parameter $\left|\Delta n_e^K / \delta n_e^{(0)}\right|$ in our perturbation expansion and is consistent with the formal expansion procedure in Ref. 11. The parallel electric field in Eq.(16) is determined by Eq.(8) for the electrostatic field and Eq.(12) for the electromagnetic contribution. The last terms on the right side of Eq.(17) arise from the electron inertia terms in Eq.(12),

$-n_{0e}m_e(\partial/\partial t + \vec{v}_{\mathbf{E}\times\mathbf{B}})u_{\|e}$. To accommodate the electron inertia terms, we used an explicit uncentered finite difference in time in the predictor step of the predictor-corrector time integration of Eqs.(13-16). With the exception of the electron inertia terms, the predictor-corrector integration of the entire system is second-order accurate in time. Retention or omission of the electron inertia terms had no significant influence the simulations. Our attempts so far to include electron subcycling in the hybrid schemes have led to numerical instability and no electron orbit-averaging[15] has been undertaken. Because of the partial linearization[3,4] no parallel electric field wave trapping of ions or electrons is allowed (however, the **E×B** kinetic trapping nonlinearity is retained), and $v_{\|}$ is a constant for both species

III. TEST SIMULATIONS

In this section we review the results of test simulations with the Hybrid II algorithm. The test cases considered are kinetic shear-Alfvén waves (including electron Landau damping), the collisionless-drift instability, and the ion-temperature-gradient instability.

A. Simulations of small-amplitude waves

With a finite-β ordering, $\beta_e m_i/m_e \geq 1$, the electrons are dominantly adiabatic but have important nonadiabatic kinetic corrections in their dielectric response. Shear-Alfvén waves and magnetized sound waves are the two fluid normal modes in a slab geometry with a uniform plasma, $k_{\|} << k$ and $\omega << \Omega_i << \Omega_e$, where $k_{\|}$ is the wavenumber component parallel to the equilibrium field and $\Omega_{e,i}$ are the electron and ion cyclotron frequencies. In Figure 1 we present a comparison of the results of the Hybrid II simulations of kinetic shear-Alfvén waves and linear theory. Plotted are scans of *Re* ω/Ω_i and *Im* ω/Ω_i vs. β_e for $k_y\rho_s = \pi/8$, $T_e = T_i$, $B_y^{(0)}/B_0 = 0.01$, $\rho_s = 2\Delta y$, and a 32×32 grid. Hybrid II results are denoted with "o" and Hybrid III (see Ref. 1) results with "x". The dashed curve is linear theory. The agreement with theory is excellent

when $\beta_e m_i / m_e > 1$. The hybrid algorithms become unstable for $\beta_e m_i / m_e < 1$; these algorithms cannot recover the electrostatic limit because of the "backwards" solution of Eq.(14). There is no requirement that the skin depth be resolved. These results resemble those obtained in the independent work of Lin and Chen.[11]

The Hybrid II algorithm yielded very good results for the collisionless drift-wave instability. In Fig. 2 we plot $Re\omega/\Omega_i$ and growth rates $Im\omega/\Omega_i$ from Hybrid II and conventional δf simulations vs. β_e and $\omega_{pe}\Delta y/c$ for $k_y\rho_s = \pi/4$, $\rho_s/L_n = 0.2$, $T_e=T_i$, $B_y^{(0)}/B_0=0.01$, $\rho_s=2\Delta y$, 16×16 grid, no magnetic shear, and only the (0,1) mode retained. The standard δf simulation described in Refs. 1 and 8 gave good results only for $\beta m_i/m_e \le O(1)$ and $\Delta y<c/\omega_{pe}$, while the Hybrid II algorithm gave good results for $\beta m_i/m_e > 1$ and any skin depth.

The Hybrid II algorithm also yielded very good results for δf slab simulations of unsheared ion-temperature-gradient instability (ITG) and was able to accommodate finite η_e. In Fig. 3 we present results from Hybrid II simulations of ITG for a single linear mode with $k_y\rho_s \approx \pi/8$, $\rho_s=2\Delta x$, 32×32 grid, no magnetic shear, $B_y^{(0)}/B_0=0.01$, $T_e=T_i$, $\eta_e=\eta_i=4$, $\rho_s/L_n=0.1$, $\Omega_e/\omega_{pe}=1$, and $m_i/m_e=1836$. The Hybrid II simulations of unsheared ITG agree well with theory for $\beta m_i/m_e > 1$, and there is no constraint on the skin depth, c/ω_{pe}, relative to the cell size Δx. Linear theory is indicated by the dashed curve in Fig. 3.

B. Nonlinear Simulations of the Ion-Temperature-Gradient Instability

Previous simulation work[1,4,5,7-9] has concluded that the slab, multi-scale physics model with kinetic electrons and ions presented here should lead to saturated states with the radial modes[5,8,9] playing an important role. In Figs. 4 and 5 we present results of nonlinear simulations of ITG instability performed with the conventional δf and Hybrid II algorithms showing linear growth followed by nonlinear saturation mediated by the nonlinear generation of radial modes

(k_y=0, $k_x \neq 0$). Nonlinear, many-mode, two-dimensional slab simulation results with no shear, $B_y^{(0)}/B_0$=0.01, T_e=T_i, η_i =η_e=4, ρ_s/L_n=0.1, Ω_e/ω_{pe}=1, m_i/m_e=1836, ρ_s=Δx, 16×16 grid, and $\Delta t c_s/L_T$=0.4 are presented. Super-gaussian k-space smoothing, exp(-k^4a^4), was used in the conventional δf code, and a Heaviside-function was used in the Hybrid II algorithm (modes were suppressed completely for k^2a^2>1, with a=1 in both algorithms). When super-gaussian smoothing was used in the Hybrid II algorithm, the shortest wavelength modes ($k\ \rho_i > 1$) affected by the filter (but not completely suppressed) were numerically unstable. We believe that this numerical instability is related to the instability observed when $\beta_e m_i / m_e < 1$ in all of the hybrid algorithms,[1] which is associated with the backwards solution of Ampere's law in Eq.(14) that becomes ill-posed in the electrostatic limit. With adequate filtering, the ITG instability saturates in the simulations; and the thermal flux across the pressure gradient and the linear growth rates decrease together as a function of increasing β_e consistent with the quasilinear argument in Ref. 9. Figure 4 shows the time histories of the fastest growing linear mode and the cross-field ion thermal flux. Figure 5 displays the accompanying mode energy spectrum at saturation showing the dominance of the radial mode and that an inverse cascade to longer wavelengths has occurred in these small simulations. The ion thermal fluxes (not time-averaged or filtered) exhibit bursts of transport often seen in ITG simulations. In sum, the Hybrid II nonlinear simulations of the ITG instability exhibit well-behaved saturated states and yield credible physics results.

IV. TOROIDAL FLUX-TUBE HYBRID II FORMULATION

Here we give the extension of the Hybrid II algorithm to a toroidal flux-tube geometry. The parallel electric field is determined from the modified electron momentum equation (Ohm's law) including toroidicity[16]

$$en_{0e}\vec{E}\ \hat{b}^{(0)} = -\ _{\|}P_{\|e} + \frac{\delta\vec{B}}{B}\quad en_{0e}\phi - n_{0e}m_e(\partial/\partial t + \vec{v}_{ExB}\quad)u_{\|e}$$

$$-\left(\tfrac{1}{2}\delta P\ _e - \delta P_{\|e}\right)\hat{b}^{(0)}\quad \ln B \tag{18}$$

where $_{\|}P_{\|e} =\ _{\|}P_{\|e}^{(0)} + T_{\|e}^{(0)}\ _{\|}(\delta n_e - \Delta n_e^K) + n_{0e}\ _{\|}\delta T_{\|e}$ with $_{\|}(T_{\|e}^{(eq)} + \delta T_{\|e}) = 0$. The Ohm's law is then used to advance $A_{\|}$ in time, $\partial A_{\|}/c\,\partial t = (\vec{E} + \quad\phi)\ \hat{b}^{(0)} = ...$ With the updated $A_{\|}$ we use Ampere's law to determine the parallel electron flux from Eq.(14) as in the slab algorithm. The electron continuity equation including magnetic curvature is next used to advance the total electron density:

$$\frac{\partial\delta n_e}{\partial t} + n_{0e}(\vec{B}^{(0)} + \delta\vec{B}\ )\quad \frac{u_{\|e}}{B} + \vec{v}_{E\times B}\quad n_e$$

$$+\frac{1}{m_e\Omega_e B^2}(\vec{B}\times\quad B)\quad (\tfrac{1}{2}\delta P\ _e + \delta P_{\|e}) + \frac{2n_{0e}}{B^3}(\vec{B}\times\quad B)\quad \phi = 0\,, \tag{19}$$

where $\Omega_s \equiv q_s B_0/m_s c$. The electric potential ϕ is determined from the quasineutrality relation Eq.(8a) using the updated electron and ion densities.

The equations of motion for the gyrokinetic ions and the drift-kinetic electrons are extended from Eqs.(11) and (16) to include both mirroring and the toroidal drifts as part of the guiding center drifts $\vec{v}_{gs}$: $\vec{v}_{gs} = v_{\|}\hat{b} + \vec{v}_{E\times B} + \vec{v}_{ds}$, $\vec{v}_{ds} = (v_{\|}^2 + v^2/2)\vec{B}\times\quad B/\Omega_s B^2$ with

$$\dot{v}_{\|} = (q_s/m_s)\hat{b}\quad\vec{E} - (\mu_s/m_s)\hat{b}\quad B + v_{\|}(\hat{b}\quad\hat{b})\ \vec{v}_{E\times B}, \tag{20}$$

where $\vec{v}_{E\times B}$ is the $E\times B$ drift velocity and gyro-averaging of the ions is included in the standard way.[10,12-14,16] In a partially linearized implementation, the first and third terms on the right side of Eq.(20) are suppressed if there are no equilibrium electric fields. The gyrokinetic equation for the ions yields the following equation for the ion weights in toroidal geometry[10]

$$\frac{d}{dt} w_i^i = -\vec{v}_{gi} \quad \ln F_M^i - \dot{\varepsilon} \frac{\partial}{\partial \varepsilon} \ln F_M^i \tag{21}$$

where ε is the particle energy and $\dot{\varepsilon} = e v_{\|} \hat{b} \;\; \vec{E} + m_i \vec{v}_{E\times B} \;\; [v_{\|}^2 \hat{b} \quad \hat{b} + (v^2/2) \quad \ln B]$. From the drift-kinetic equation for electrons with split-weights (after cancellations obtained by using Ohm's law and the continuity equation)

$$\frac{d}{dt} w_i^e = (\kappa_e - \kappa_{ne}) \hat{x} \;\; (\vec{v}_{E\times B} + v_{\|} \hat{b}) - \vec{v}_{de} \quad \delta n_e / n_{0e} + \vec{B} \quad (u_{\|e} / B) + (v_{\|} / v_e^2)(\frac{\partial}{\partial t} + \vec{v}_{E\times B} \quad) u_{\|e}$$

$$+ v_{\|} (\hat{b}^{(0)} \quad \ln B)(\tfrac{1}{2} \delta p_{\;e} - \delta p_{\|e}) / (n_{0e} T_e^{(0)}) + \vec{v}_{E\times B} \;\; (\varepsilon_{\|} \hat{b} \quad \hat{b} + \tfrac{1}{2} \varepsilon \quad \ln B) / T_e^{(0)}$$

$$+ (n_{0e} m_e \Omega_e B^2)(\vec{B} \times \quad B) \quad (\delta p_{\|e} + \tfrac{1}{2} \delta p_{\;e}) + (2c/B^3)(\vec{B} \times \quad B) \quad \phi \tag{22}$$

Flux-tube coordinates are used with the following definitions:[10] $x = r - r_0$, $y = (r_0/q_0)(q\theta - \zeta)$, $z = q_0 R_0 \theta$. Implementation of these equations in a code is underway.

IV. TIME-STEP, ACCURACY AND CONVERGENCE CONSIDERATIONS

For kinetic simulations to provide credible results there are a number of accuracy issues that restrict the time steps and grid resolution used:

$$k \;\; v_{\mathbf{E}\times\mathbf{B}} \Delta t < 1 \;\; k \;\; \Delta x \quad < 1 \;\; k_{\|} \Delta x_{\|} < 1 \quad \omega \Delta t < 1 \quad \Delta x \quad \le \rho_{i,s} \quad k_{\|} v_s \Delta t < 1 \tag{23}$$

where $v_s = (T_s/m_s)^{1/2}$ is the thermal velocity for each species. The first condition in (23) is representative of a restriction on resolving finite-amplitude phenomena. There is also the stability constraint set by $k_{\|} v_A \Delta t < 1$ for $v_A > c_s$. Taking into account that $\Delta x_{\|} = (B_0 / B_y^{(0)}) \Delta y \equiv \theta^{-1} \Delta y$ in the two-dimensional slab, the Alfvén stability condition is $\theta v_A \Delta t / \Delta y < 1$. We note that $v_e / v_A = (\beta_e m_i / m_e)^{1/2}$ and $v_i / v_A = (\beta_e T_i / T_e)^{1/2}$.

We have demonstrated that in the conventional δf simulation there is a constraint on resolving the skin depth c/ω_{pe} with the grid spacing in order to accurately reproduce the linear dispersion relation of shear-Alfvén waves and the drift instabilities.[1] Because

$\rho_i/(c/\omega_{pe}) = (T_i/T_e)^{1/2}(\beta m_i/m_e)^{1/2}$, the skin depth c/ω_{pe} becomes smaller than $\rho_i \sim \rho_s$ when $\beta_e m_i/m_e > 1$. Note that c/ω_{pe}=0.05 cm for n_e=10^{14}/cm^3. Thus, resolving the skin depth becomes a more severe and onerous constraint than $\Delta x \leq \rho_s$ for $\beta_e m_i/m_e > 1$. The Hybrid II algorithm is not constrained to resolve the skin depth with the spatial grid, but it behaves well only for $\beta_e m_i/m_e \geq 1$. With magnetic shear (not addressed here), populating the resonant electron layer with particles can become an additional important accuracy constraint on the simulations:[9] $\Delta x_e \equiv (k_{||}/k_y)L_s \sim (\omega/k_y v_e)L_s \sim (m_e/m_i)^{1/2}(L_s/L_n)\rho_s$.

With $v_e\Delta t_e/\Delta x_{||} \leq O(1)$ our simulations are well-behaved, and self-heating and numerical diffusion of the electron velocity distribution are acceptably small.[17,18] In Figure 6 we show results for Hybrid II simulations of the ITG and collisionless-drift instabilities in which the frequencies and growth rates of a single small-amplitude mode are plotted as a function of time step in the simulation. Hybrid II simulations of ITG retain some sensitivity to electron kinetics: $v_e\Delta t/\Delta y_{||} \leq 1.5$ is needed for accurate simulations of a system with η_i=η_e=4, β_e=0.035, 32×32 grid, m_i/m_e=1837, $k_y\rho_s$=π/8, θ=0.01, ρ_s/L_n=0.1, and no magnetic shear; and we note that there is no electron subcycling. The collisionless drift wave is more sensitive to electron kinetics: $v_e\Delta t/\Delta y_{||} \leq 0.3$ is needed to accurately simulate a system with β_e=0.0049, 16×16 grid, m_i/m_e=1837, $k_y\rho_s$=π/4, θ=0.01, ρ_s/L_n=0.2, and no magnetic shear.

The convergence of nonlinear simulations of drift-wave instability driven transport may set the most restrictive condition on time step, and the time step may depend on the parameters and physical conditions of the particular problem.[19] We consider examples in Fig. 7 of nonlinear, many-mode, two-dimensional slab Hybrid II simulations as a function of time step. The simulation parameters were $\Delta t c_s/L_T$=0.4, 0.2, 0.1; β_e=2.2×10^{-3}; no magnetic shear; θ=0.01;

$T_e=T_I$; $\eta_i=\eta_e=4$; $\rho_s/L_n=0.1$; $\Omega_e/\omega_{pe}=1$; $m_i/m_e=1836$; $\rho_s=\Delta x$; 16×16 grid; and Heaviside-function mode filtering with a=1. For these parameters we can relate $\Delta t c_s/L_T$ to $v_e\Delta t/\Delta y_{||}$: $\Delta t c_s/L_T=(\Delta y/L_T)(m_e/m_i)\left(B_0/B_y^{(0)}\right)v_e\Delta t/\Delta y_{||}\approx 0.2 v_e\Delta t/\Delta y_{||}$. If the time step is not chosen adequately small to resolve the nonlinear physics, there is a slow, secular, residual growth of the electrostatic and vector potential mode energies and a concomitant slow growth of the averaged cross-field thermal fluxes that in the supposedly saturated state. The accuracy constraints on the linear dispersion for ITG and collisionless drift-wave simulations in Fig. 6 set time step conditions $v_e\Delta t/\Delta y_{||}<0.5$ that translate into $\Delta t c_s/L_T<0.1$. These time steps are in keeping with the converged results for the nonlinear simulations in Fig. 7 and within the range of time steps typically used for the nonlinear toroidal gyrokinetic simulations in Ref. 19 which had gyrokinetic ions and adiabatic electrons. The experience presented here is encouraging for the addition of kinetic electrons and electromagnetic coupling to toroidal gyrokinetic simulations. However, we note that there are additional considerations that can influence the time step in toroidal simulations, which are not addressed here.

We next consider nonlinear, many-mode slab simulations in Fig. 8 with increasing box size (16×16, 32×32, 64×64) with $\beta_e=2.2\times10^{-3}$, no shear, θ=0.01, $T_e=T_i$, $\eta_i=\eta_e=4$, $\rho_s/L_n=0.1$, $\Omega_e/\omega_{pe}=1$, $m_i/m_e=1836$, $\rho_s=\Delta x$, Heaviside-function filtering in Hybrid II algorithm: $a_x=a_y=1$. These simulations all saturate and are well behaved with credible physics results. The physics results are influenced by the inclusion of longer wavelength modes and the decreased spacing between the modes in k space.

Statistical convergence with respect to both electrons and ions must be examined with the inclusion of kinetic electron and electromagnetic effects. In Fig. 9 we compare the results of

nonlinear, many-mode slab simulations vs. particles per cell with $\beta_e = 2.2 \times 10^{-3}$, no shear, θ=0.01, $T_e = T_i$, $\eta_i = \eta_e = 4$, $\rho_s / L_n = 0.1$, $\Omega_e / \omega_{pe} = 1$, $m_i / m_e = 1836$, $\rho_s = \Delta x$, 64×64 grid, Heaviside-function filtering in Hybrid II algorithm: $a_x = a_y = 1$. Increasing the number of particles per cell led to a well-behaved saturation. When under-resolved with respect to particles, the simulations did not saturate properly.

V. CONCLUSION

Including both electron and ion kinetic effects using a realistic mass ratio and accommodating a low-frequency electromagnetic model of the self-consistent electromagnetic fields in the plasma add significant complexity to drift-wave turbulence simulation models. The algorithm studied here attempts to capture the physics of low-frequency ($\omega << \Omega_i$) drift-wave phenomena, the coupling to kinetic Alfvén waves that occurs at finite plasma pressure, and linear and nonlinear electron and ion kinetic phenomena (e.g., Landau resonance, particle trapping, induced Compton scattering).

The results presented indicate that significant progress is being made in adding kinetic electron and electromagnetic effects to multi-dimensional gyrokinetic ion simulations of core turbulent transport. The Hybrid II algorithm yields good results for finite β_e, $\beta_e m_i / m_e > 1$, and does *not* require that the cell size be smaller than the skin depth c/ω_{pe}, but leads to a numerical instability for $\beta_e m_i / m_e < 1$. Both the conventional δf and kinetic-extended hybrid algorithms have restrictions on the time step used and the statistical and spatial resolution needed to recover the correct dielectric responses and to produce converged nonlinear steady states. Similar non-dimensional time steps are required in three-dimensional nonlinear toroidal gyrokinetic simulations with adiabatic electrons. Simulation examples of linear and nonlinear wave phenomena have been presented that establish the utility of the Hybrid II algorithm.

Acknowledgments

This work was supported by the U.S. Department of Energy under Contract No. W-7405-ENG-48 at the University of California Lawrence Livermore National Laboratory. We thank J.-N. Leboeuf, L. Chen, G. Hammett, P. Snyder, W. Lee, and Z. Lin for useful discussions. This research is a part of the SciDAC Plasma Microturbulence Project sponsored by the DOE Office of Fusion Energy Sciences.

References

[1]B.I. Cohen, A.M. Dimits, W.M. Nevins, Y. Chen, and S.E. Parker, "Kinetic Electron Closures for Electromagnetic Simulation of Drift and Shear-Alfvén Waves (I)", submitted to Physics of Plasmas.

[2]Y. Chen and S. Parker, Phys. Plasmas **8**, 441 (2001).

[3]M. Kotschenreuther, Bull. Am. Phys. Soc. **34**, 2107 (1988); R. E. Denton and M. Kotschenreuther, J. Comput. Phys. **119**, 283 (1995).

[4]A. M. Dimits and W. W. Lee, J. Comput. Phys. **107**, 309 (1993).

[5]B. I. Cohen, T. J. Williams, A. M. Dimits, and J. A. Byers, Phys. Fluids B **5**, 2967 (1993).

[6]I. Manuilsky and W. W. Lee, Phys. Plasmas **7**, 1381 (2000).

[7]J. V. W. Reynders, Ph.D. thesis, Princeton University (1992).

[8]J. C. Cummings, Ph.D. thesis, Princeton University (1995).

[9]B. I. Cohen and A. M. Dimits, Phys. Rev. E **56**, 2151 (1997).

[10]Y. Chen and S. E. Parker, Phys. Plasmas **8**, 2095 (2001).

[11]Z. Lin and L. Chen, Phys. Plasmas **8**, 1447(2001).

[12]T. S. Hahm, W. W. Lee, and A. Brizard, Phys. Fluids **31**, 1940 (1988).

[13]E. A. Frieman and L. Chen, Phys. Fluids **25**, 502 (1982).

[14]W. W. Lee, Phys. Fluids **26**, 556 (1983); W.W. Lee, J. Comput. Phys. **72**, 243 (1987).

[15]B. I. Cohen, T. A. Brengle, D. B. Conley, and R. P. Freis, J. Comp. Phys. 38, 45 (1980); B. J.U. Brackbill and B.I. Cohen, *Multiple Time Scales* , Computational Techniques (Academic Press Inc., Orlando, 1985), Chapt. 10.

[16] S.E. Parker, J.C. Cummings, W.W. Lee and H.E. Mynick, in *Joint Varenna-Lausanne 15th International Workshop on Theory of Fusion Plasmas*, August 22-26, 1994 (Editrice Composotori for Intaliana di Fisica, Bologna, 1994)]; P. B. Snyder, Ph.D. thesis, Princeton U.,

1999; P.B. Snyder and G.W. Hammett, Phys. Plasmas **8**, 744 (2001).

[17]C. K. Birdsall and A. B. Langdon, *Plasma Physics Via Computer Simulation* (McGraw-Hill, New York, 1985), Ch. 8.

[18]A. B. Langdon, J. Comput. Phys. **30**, 202 (1979).

[19]A. M. Dimits, G. Bateman, M. A. Beer, B. I. Cohen, W. Dorland, G. W. Hammett, C. Kim, J. E. Kinsey, M. Kotschenreuther, A. H. Kritz, L. L. Lao, J. Mandrekas, W. M. Nevins, S. E. Parker, A. J. Redd, D. E. Shumaker, R. Sydora, and J. Weiland, Phys. Plasmas **7**, 969 (2000).

Figure Captions

Figure 1. Frequencies and damping rates from Hybrid II (o) and III (x) simulations of kinetic shear-Alfvén waves as functions of the electron β_e.

Figure 2. Frequencies and growth rates from Hybrid II ( ) and conventional δf (o) simulations of the collisionless drift-wave instability as functions of the ratio of the cell size to the skin depth and the electron β_e.

Figure 3. Frequencies and growth rates from Hybrid II simulations (with η_e=4) of the ion-temperature-gradient instability as functions of the electron β_e.

Figure 4. The spatially averaged ion thermal fluxes in x normalized to the sound speed and the modulus of the Fourier amplitude of the electric potential for the fastest growing mode from conventional δf and Hybrid II nonlinear simulations of the ion-temperature-gradient instability as functions of time for three simulations at different values of β_e.

Figure 5. The modulus of the Fourier amplitude of the electric potential as a function of k_y for k_x=1 (both normalized to $\Delta k \equiv \pi / 8$) averaged in time after saturation in three δf and Hybrid II nonlinear simulations of the ion-temperature-gradient instability for different values of β_e.

Figure 6. Frequencies and growth rates from Hybrid II simulations of the ion-temperature-gradient and collisionless drift-wave instabilities as functions of the relative time step.

Figure 7. The spatially averaged ion thermal fluxes in x normalized to the sound speed and the modulus of the Fourier amplitude of the electric potential for the fastest growing mode from conventional Hybrid II nonlinear simulations of the ion-temperature-gradient instability as functions of time for three simulations at different values of the relative time step. The observed linear growth rates are indicated.

Figure 8. Nonlinear slab simulations of ITG instability: time histories of the cross-field ion thermal fluxes and the fluctuation spectrum at the end of the simulation in k_y for the electric potential as a function of increasing box size in two dimensions.

Figure 9. Nonlinear two-dimensional slab simulations of ITG instability: time histories of the cross-field ion thermal fluxes and a single Fourier mode of the electric potential as a function of the number of particles per cell for each species.

Figure 1

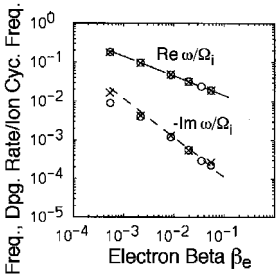
Freq., Dpg. Rate/Ion Cyc. Freq.
10^0
10^{-1}
10^{-2}
10^{-3}
10^{-4}
10^{-5}
Re ω/Ω_i
-Im ω/Ω_i
10^{-4}
10^{-3}
10^{-2}
10^{-1}
Electron Beta β_e

Figure 2

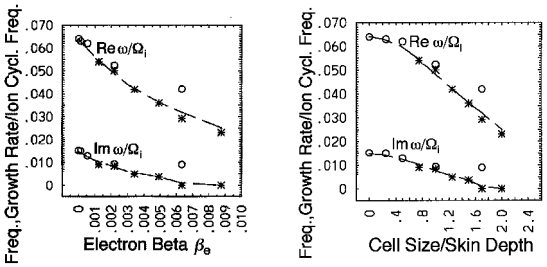
Freq.,Growth Rate/Ion Cycl. Freq.
.070
.060
.050
.040
.030
.020
.010
0
Re ω/Ω_i
Im ω/Ω_i
0
.001
.002
.003
.004
.005
.006
.007
.008
.009
.010
Electron Beta β_e
Freq.,Growth Rate/Ion Cycl. Freq.
.070
.060
.050
.040
.030
.020
.010
0
Re ω/Ω_i
Im ω/Ω_i
0
.4
.8
1.2
1.6
2.0
2.4
Cell Size/Skin Depth

Figure 3

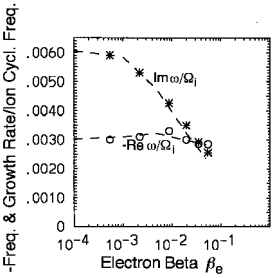
-Freq. & Growth Rate/Ion Cycl. Freq.
.0060
.0050
.0040
.0030
.0020
.0010
0
Im ω/Ω_i
-Re ω/Ω_i
10^-4
10^-3
10^-2
10^-1
Electron Beta β_e

Figure 4

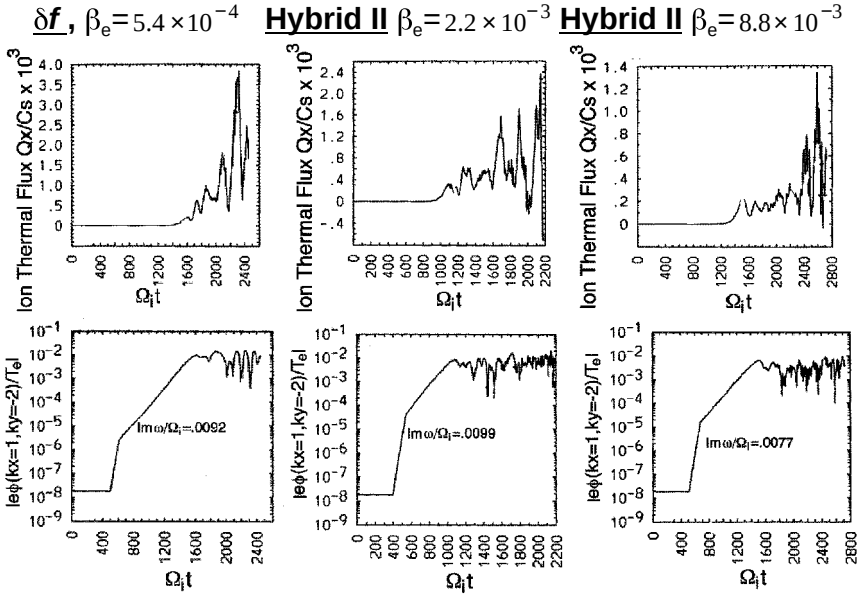
δf , βe=5.4×10−4
Hybrid II βe=2.2×10−3
Hybrid II βe=8.8×10−3
Ion Thermal Flux Qx/Cs x 10^3
Ωit
|eϕ(kx=1,ky=-2)/Te|
Imω/Ωi=.0092
Imω/Ωi=.0099
Imω/Ωi=.0077

Figure 5

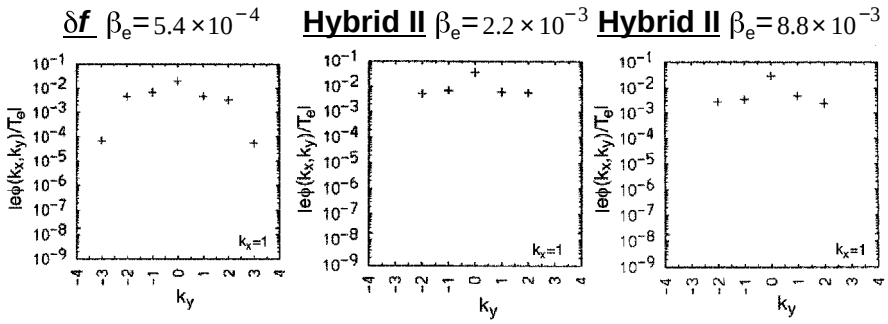
δf βe=5.4×10−4
Hybrid II βe=2.2×10−3
Hybrid II βe=8.8×10−3
|eφ(kx,ky)/Te|
ky
kx=1

Figure 6

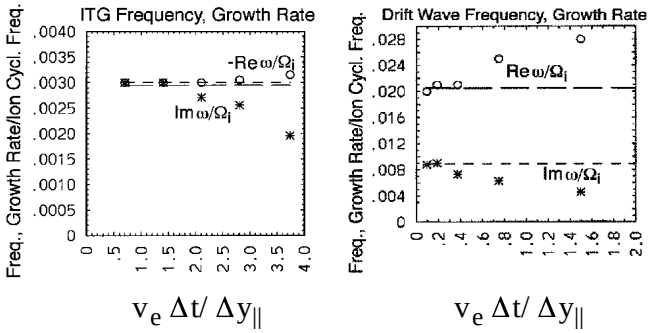
ITG Frequency, Growth Rate
Freq., Growth Rate/Ion Cycl. Freq.
-Re ω/Ω_i
Im ω/Ω_i
.0040
.0035
.0030
.0025
.0020
.0015
.0010
.0005
0
0
.5
1.0
1.5
2.0
2.5
3.0
3.5
4.0
v_e Δt/ Δy_||
Drift Wave Frequency, Growth Rate
Freq., Growth Rate/Ion Cycl. Freq.
Re ω/Ω_i
Im ω/Ω_i
.028
.024
.020
.016
.012
.008
.004
0
0
.2
.4
.6
.8
1.0
1.2
1.4
1.6
1.8
2.0
v_e Δt/ Δy_||

Figure 7

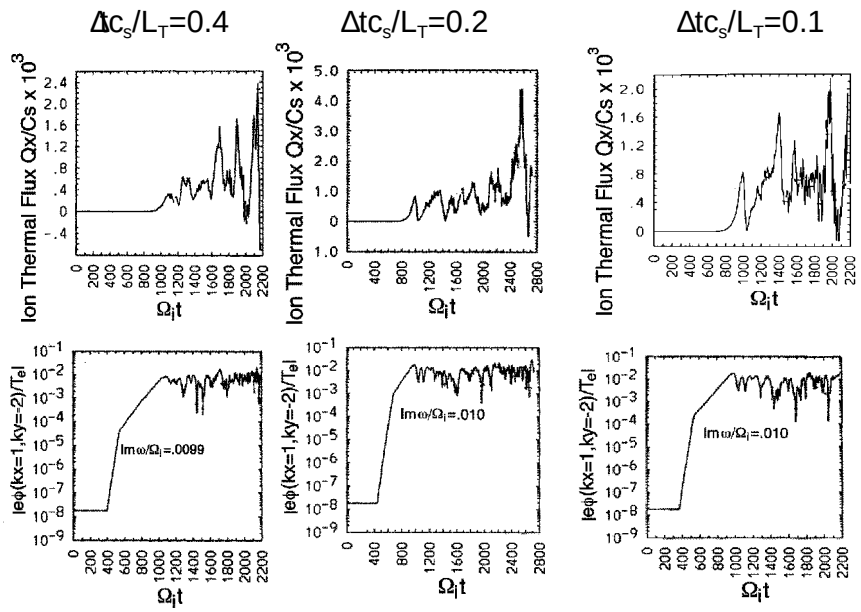
Δtc_s/L_T=0.4
Δtc_s/L_T=0.2
Δtc_s/L_T=0.1
Ion Thermal Flux Qx/Cs x 10^3
Ω_i t
|eφ(kx=1,ky=-2)/T_el|
Imω/Ω_i=.0099
Imω/Ω_i=.010
Imω/Ω_i=.010

Figure 8

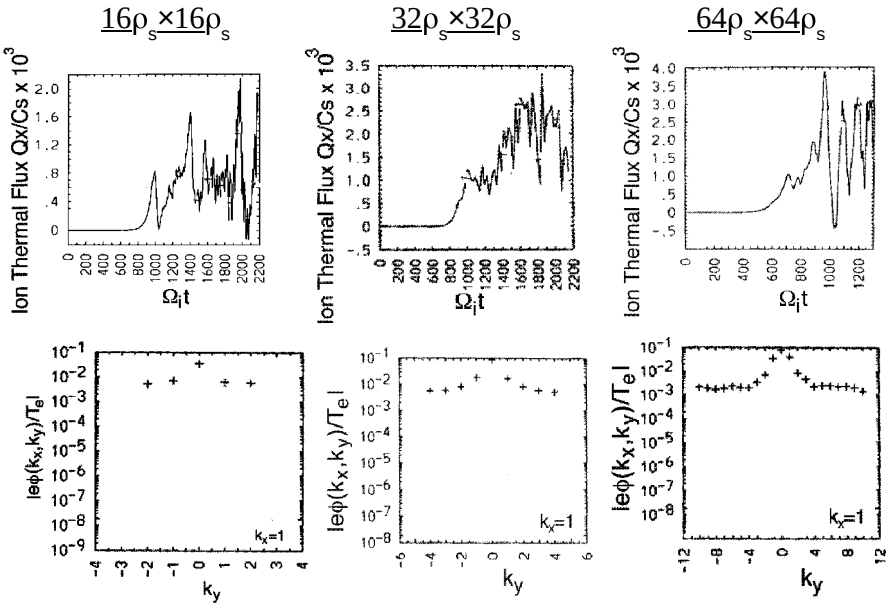
16ρs×16ρs
32ρs×32ρs
64ρs×64ρs
Ion Thermal Flux Qx/Cs x 10^3
Ωit
|eφ(kx,ky)/Te|
kx=1
ky

Figure 9

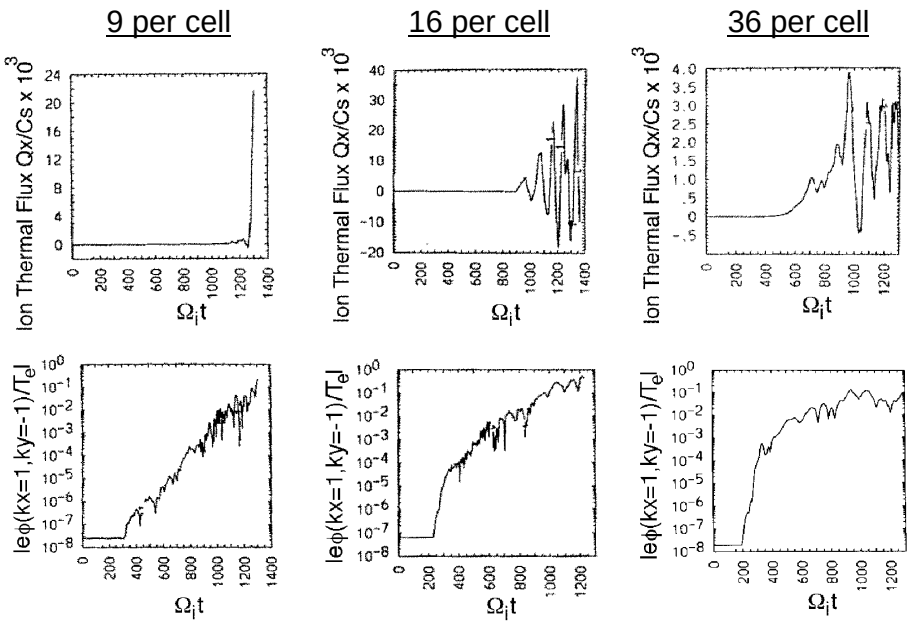
9 per cell
16 per cell
36 per cell
Ion Thermal Flux Qx/Cs x 10^3
Ωit
|eφ(kx=1,ky=-1)/Te|